

Tailored PEDOT:PSS phase segregation for high-efficiency flexible all-perovskite tandem solar cells and mini-modules

Received: 17 April 2025

Accepted: 9 November 2025

Published online: 11 December 2025

Check for updates

Huagui Lai¹, Jingwei Zhu², Rui-Tung Kuo³, Urs Aeberhard⁴, Zhan-Hong Lin⁵, Nada Mrkyvkova^{6,7}, Jincheng Luo¹, Severin Siegrist¹, Philipp Wechsler¹, Chih-Jen Shih⁵, Peter Siffalovic^{6,7}, Cong Chen^{1,2}, Ayodhya Nath Tiwari¹, Tzu-Ying Lin³✉, Dewei Zhao²✉ & Fan Fu¹✉

Flexible all-perovskite tandem solar cells (TSCs) promise lightweight power for portable and aerospace uses, yet performance remains limited by interfacial losses in narrow-bandgap (NBG) sub-cells, particularly arising from poly(3,4-ethylenedioxythiophene):poly(styrene sulfonate) (PEDOT:PSS). Here, we uncover a previously unrecognized vertical phase segregation in PEDOT:PSS films, with an insulating PSS-rich surface layer atop a conductive PEDOT-rich base. This architecture induces interfacial electric dipoles that hinder efficient hole extraction. We find that the inclusion of Triton X-100 disrupts this segregation by modulating polymer interactions, thereby suppressing surface dipole formation. NBG perovskite cells incorporating this modified interface exhibit enhanced performance and reproducibility. This strategy enables flexible TSCs with a power conversion efficiency (PCE) of 25.4% and a proof-of-concept flexible tandem solar mini-module reaches 19.7%, with theoretical modeling projecting module efficiencies exceeding 24%. These results provide key insights into PEDOT:PSS interfacial phenomena and elucidate design principles for optimizing interfaces for next-generation flexible perovskite tandems.

All-perovskite tandem solar cells (TSCs) offer a promising route to surpass the efficiency limits of single-junction devices^{1,2}, with certified power conversion efficiencies (PCEs) exceeding 30% on rigid substrates³. Their flexible counterparts offer additional advantages, especially a high power-to-weight ratio, making them particularly attractive for applications in portable electronics, building-integrated photovoltaics, and aerospace systems^{4,5}. Despite these benefits, flexible TSCs still lag behind rigid devices, with reported PCEs below 25%^{6,7}.

One critical barrier lies in the fabrication of efficient narrow-bandgap (NBG) perovskite solar cells (PSCs) on non-planar, flexible substrates.

To achieve high-performance flexible TSCs, both the wide-bandgap (WBG) and NBG PSCs require conformal and high-quality hole transport layers (HTLs). While recent advances—such as self-assembled monolayers (SAMs) and NiO_x interlayers—have improved HTL interfaces in WBG PSCs^{6–8}, the NBG PSCs still rely heavily on poly(3,4-ethylenedioxythiophene) polystyrene sulfonate (PEDOT:PSS).

¹Laboratory for Thin Films and Photovoltaics, Empa - Swiss Federal Laboratories for Materials Science and Technology, Dübendorf, Switzerland. ²College of Materials Science and Engineering & Engineering Research Center of Alternative Energy Materials & Devices, Ministry of Education, Sichuan University, Chengdu, China. ³Department of Materials Science and Engineering, National Tsing Hua University, Hsinchu, Taiwan. ⁴Fluxim AG, Katharina-Sulzer-Platz 2, Winterthur, Switzerland. ⁵Institute for Chemical and Bioengineering, ETH Zürich, Zürich, Switzerland. ⁶Center for Advanced Materials Application, Slovak Academy of Sciences, Bratislava, Slovakia. ⁷Institute of Physics, Slovak Academy of Sciences, Bratislava, Slovakia. ✉e-mail: tzuying.lin@mx.nthu.edu.tw; dewei.zhao@scu.edu.cn; dewei_zhao@hotmail.com; fan.fu@empa.ch

Despite its compatibility with solution processing, PEDOT:PSS presents two major challenges in flexible devices: difficulty in forming uniform ultrathin coatings and phase segregation that leads to insulating, hygroscopic PSS accumulation^{9,10}. These limitations compromise film uniformity, interfacial quality, and ultimately, device reproducibility and performance.

Although PEDOT:PSS has often been assumed to adopt a “pancake” morphology composed of PEDOT-rich cores surrounded by PSS-rich shells, this structural model—supported mainly by morphological studies—does not fully account for the film’s interfacial behavior^{11,12}. Due to the insulating and hygroscopic nature of PSS, many efforts have sought to remove the PSS shell within the pancake-like PEDOT:PSS film through post-deposition treatments (PDTs), such as the application of solvents (e.g., dimethyl sulfoxide (DMSO))^{13,14}, ionic liquids¹⁵, surfactants¹⁶, or acids¹⁷. Most of these studies include a washing process for the as-deposited PEDOT:PSS film and observed a reduced PSS phase and enhanced conductivity in the film. However, the underlying mechanisms driving these improvements remain unclear, and the structural properties of PEDOT:PSS films are still not fully understood^{10,13}. Furthermore, processing challenges for PEDOT:PSS films on flexible WBG PSCs persist, limiting progress in high-performance flexible TSCs.

Here, we present an additive engineering strategy to overcome these limitations by incorporating the non-ionic surfactant Triton X-100 directly into the PEDOT:PSS dispersion. Our characterization reveals a vertically segregated double-layer structure in pristine PEDOT:PSS films, with an insulating PSS-rich surface atop a conductive

PEDOT base. We hypothesize that this structure induces interfacial electric dipoles that impede charge extraction. The incorporation of Triton X-100 suppresses this surface segregation, resulting in significant enhancements in both performance and reproducibility of NBG PSCs—from an average PCE of ~14.0% to 19.9%. Integrating this strategy into flexible tandem architectures, we achieve a high PCE of 25.4%. Furthermore, leveraging simulation-assisted laser scribing, we demonstrate a proof-of-concept mini-module with 19.7% efficiency. Theoretical modeling suggests that module efficiencies above 24% are achievable on 10 cm × 10 cm flexible substrates, marking a critical step toward scalable, high-performance flexible tandem photovoltaics.

Results

Challenges in NBG PSCs and tandems

Achieving high-performance NBG PSCs with excellent uniformity is essential for the development of efficient flexible TSCs and, subsequently, tandem solar modules. However, our observations show that the processing of NBG PSCs suffers from poor reproducibility and uniformity. This issue is reflected in the PV performance of small-area devices (0.09 cm²), as shown in Fig. 1a–d. A significant spread in PV performance is observed, primarily attributed to variations in J_{SC} and FF.

During the J - V measurements, we noticed that the J_{SC} and FF of devices on the same substrate are highly dependent on the measurement sequence. The first measured cell (Cell #1) consistently exhibited higher J_{SC} and FF, whereas the last measured cell (Cell #4) showed significantly lower values. When the first cell (Cell #1) was remeasured

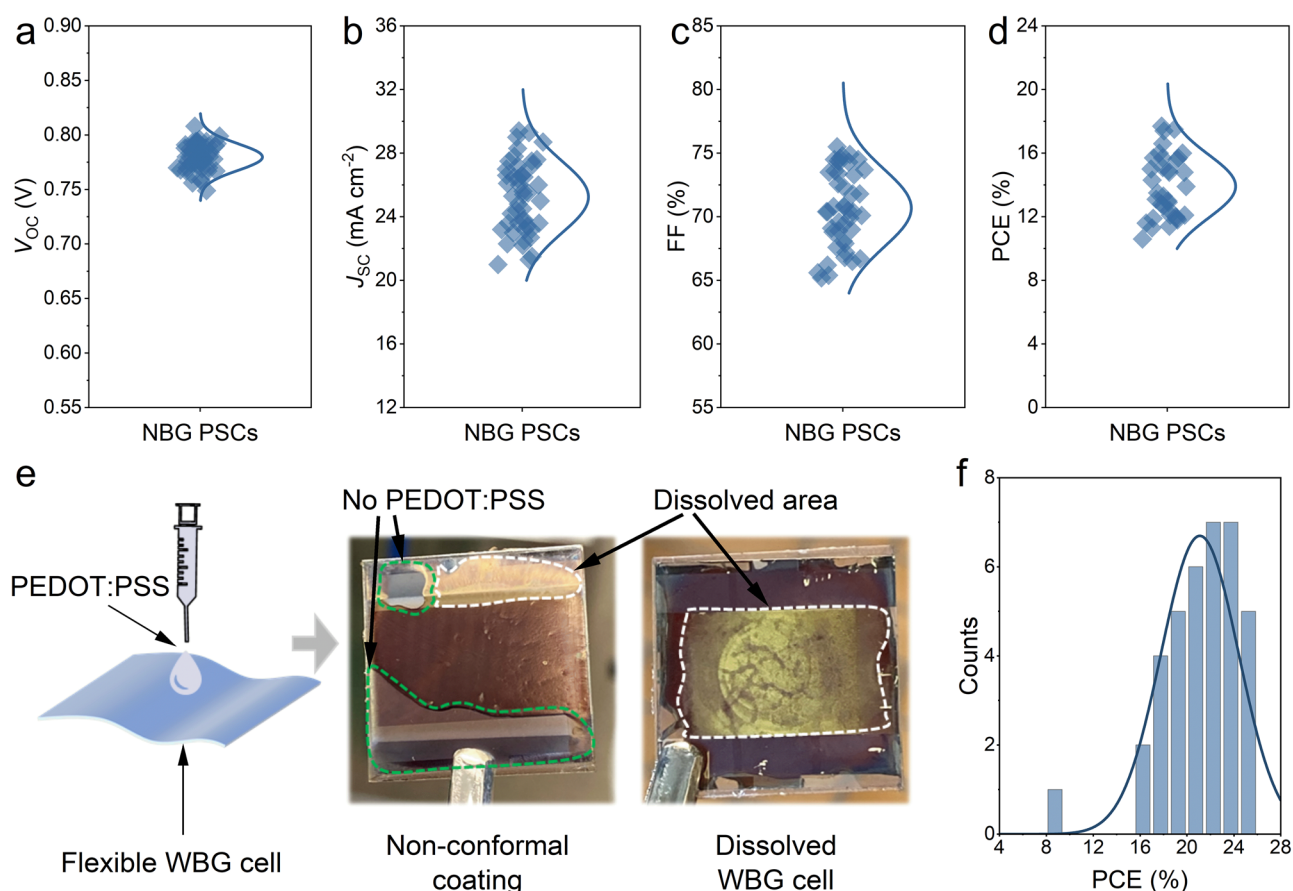


Fig. 1 | Challenges in narrow-bandgap (NBG) perovskite solar cells (PSCs) and flexible tandems. **a–d** Statistical distribution of PV parameters (V_{OC} : open-circuit voltage; J_{SC} : short-circuit current density; FF: fill factor; PCE: power conversion efficiency) represented in box plots for NBG PSCs, 50 cells included. **e** Schematics show the spin-coating of PEDOT:PSS dispersion onto the flexible wide-bandgap

(WBG) cell and photos of the failed samples. **f** Histograms showing the PCEs of 17 flexible TSCs, fitted with a Gaussian function (solid line). Area without PEDOT:PSS coating is labeled with green dashed lines, and the dissolved area is labeled with white dashed lines.

after the measurement of Cell #4, it also displayed reduced J_{SC} and FF. However, the integrated J_{SC} derived from EQE measurement is much higher than that obtained from the J - V measurement (Supplementary Fig. 1). To investigate this observation further, we examined the growth of NBG perovskite film using scanning electron microscopy (SEM). The SEM images revealed no pinholes within the perovskite absorber (Supplementary Fig. 2). Based on these results, we assume photocurrent under the light-soaking conditions of J - V measurements with AM1.5 illumination to be limited by the insufficient rate of thermionic emission over interfacial barriers, while no such limitation applies for the low current density during a quantum efficiency measurement¹⁸. We hypothesize that the perovskite/PEDOT:PSS buried interface is mainly responsible for this phenomenon and, therefore, a significant spread in PV performance for our NBG PSCs.

Based on these NBG cells, flexible all-perovskite TSCs were also fabricated, using an architecture consisting of a polyethylene naphthalate (PEN) substrate with the following layer stack: ITO/(4-(7H-dibenzo[c,g]carbazol-7-yl)butyl)phosphonic acid (4PADCB)/WBG perovskite/[6,6]-phenyl-C61-butyric acid methyl ester (PCBM)/SnO_x/gold (Au)/PEDOT:PSS/NBG perovskite/C₆₀/SnO_x/copper (Cu), of which the WBG cell is based on our previous work with optimized uniformity^{7,19}. Another challenge encountered is associated with the processing of the PEDOT:PSS film, which is relatively straightforward in single-junction devices but becomes problematic in TSCs, especially on flexible substrates. As illustrated in Fig. 1e, we found that spin-coating PEDOT:PSS (Clevios™ P VP Al 4083) onto flexible WBG PSCs presents significant challenges in realizing conformal coating. The spin-coating process often results in non-conformal coatings (green dashed lines) due to the low wettability of the PEDOT:PSS dispersion or damage to the underlying WBG PSCs (white dashed lines), caused by the long interaction with the aqueous dispersion. With this non-conformal layer, the overall PV performance uniformity of the flexible TSCs was unsatisfactory, with an average PCE of around 21 to 22%, as shown in the histogram in Fig. 1f.

Triton X-100 additives in PEDOT:PSS

To optimize the coating process of PEDOT:PSS and improve the PV performance of the NBG PSCs and therefore TSCs, we developed an additive engineering strategy by introducing a non-ionic surfactant, Triton X-100, into the PEDOT:PSS dispersion. The chemical structures of PEDOT:PSS and Triton X-100 are shown in Fig. 2a. Triton X-100 features a hydrophilic polyethylene oxide chain and a hydrophobic aromatic hydrocarbon group. The hydrophilic chain interacts with PSS, while the hydrophobic group interacts with PEDOT, promoting a well-dispersed system²⁰. We first compared the wettability of PEDOT:PSS on glass/ITO substrates. Contact angle measurements, shown in Fig. 2b, revealed that adding 0.5 wt% Triton X-100 to PEDOT:PSS significantly reduced the contact angle of droplets on the glass/ITO surface, confirming improved wettability. Moreover, on flexible PEN/ITO and PEN/WBG cell surfaces, pristine PEDOT:PSS exhibits much larger contact angles, reflecting poorer wetting. The introduction of Triton X-100 effectively reduces these contact angles as well, as shown in Supplementary Fig. 3, confirming its beneficial effect on wettability across both rigid and flexible substrates. Supplementary Note 1 presents a schematic of the mechanism by which Triton X-100 enhances aqueous dispersion, along with the corresponding experimental data.

To examine its influence on perovskite growth, we compared top-view SEM images of perovskite films grown on PEDOT:PSS with and without Triton X-100, shown in Fig. 2c (see additional images in Supplementary Fig. 4). It is calculated that the perovskite film based on PEDOT:PSS with Triton X-100 exhibited an average grain size of 0.45 μm², significantly larger than the 0.18 μm² obtained in the reference group (Supplementary Fig. 5). This increase in grain size indicates a reduced concentration of perovskite seeds, which is most likely due to the modified morphology of PEDOT:PSS^{21,22}. Furthermore, the films

showed more pronounced columnar growth (Fig. 2d and Supplementary Fig. 6), which is beneficial for charge transport and collection²³. Grazing-incidence wide-angle X-ray scattering (GIWAXS) confirmed that the NBG perovskites grown on both types of PEDOT:PSS films preserved their polycrystalline structure and maintained the same crystal orientation (Supplementary Fig. 7). We then measured the time-resolved photoluminescence (TrPL) of the perovskite films deposited on different substrates. As shown in Fig. 2e, the TrPL decay curve of the film grown on PEDOT:PSS modified with Triton X-100 exhibited a faster decay compared to the reference sample, indicating improved charge carrier extraction at the PEDOT:PSS/perovskite interface (lifetime fitted in Supplementary Table 1).

We fabricated NBG PSCs using PEDOT:PSS with various concentrations of Triton X-100 (0 to 1 wt%). As shown in Supplementary Fig. 8, device performance improved across a wide concentration range (0.1–0.75 wt%), while higher concentrations (> 0.75 wt%) led to excessive spreading and lower performance. This observation confirms that Triton X-100 not only enhances wettability but also contributes to improved device performance and narrowed spreading. Furthermore, the previously observed drop in J_{SC} and FF during sequential J - V measurements has been eliminated by incorporating Triton X-100, as shown in Supplementary Fig. 9. This further supports our earlier assumption that the issue with our NBG PSCs originates from the PEDOT:PSS layer. With Triton X-100 additive in PEDOT:PSS, the champion device exhibited a PCE of 21.5% as the J - V results shown in Fig. 2f, with the measured J_{SC} closely matching the integrated J_{SC} obtained from EQE measurements (Fig. 2g). Devices with Triton X-100 also show enhanced shelf stability: under N₂-glovebox storage they retain 93.8% of the initial PCE after 1375 h, while reference devices retain only 80.7% after 100 h (Fig. 2h). The operational stability of the device was checked by maximum power point (MPP) tracking as shown in Supplementary Fig. 10, with a steady-state efficiency of ~20.7%.

Structure of PEDOT:PSS

To elucidate the mechanism by which Triton X-100 enhances the quality of PEDOT:PSS films and the performance of NBG PSCs, we conducted time-of-flight secondary ion mass spectrometry (ToF-SIMS) depth profiling on films with 0.5 wt% Triton X-100 (hereafter refer as with Triton X-100) or without Triton X-100 (hereafter refer as reference). Depth profiling of ethylene oxide fragments (C₂H₄O) characteristic of Triton X-100, revealed their localization predominantly at the bottom of the PEDOT:PSS film (Fig. 3a). In addition, depth profiles of sulfur (S) (Fig. 3b) revealed a reduced S at the surface of the film containing Triton X-100. While ToF-SIMS cannot differentiate between S originating from PEDOT or PSS, the observed reduction in S suggests a strong interaction between Triton X-100 and PEDOT or PSS, changing the film composition. To further quantify this compositional shift, we performed X-ray photoelectron spectroscopy (XPS) measurements on PEDOT:PSS films. As shown in Fig. 3c, d, raw XPS data were acquired for PEDOT:PSS films in the range of 160–174 eV (S 2p), and the fitted peaks represent sulfur atoms from the styrene sulfonate (170–166 eV, red gradients) and the EDOT thiophene (166–161 eV, navy gradients). Given that both PEDOT and PSS contain one sulfur atom per repeat unit, the surface PSS/PEDOT ratio can be directly obtained from these spectral areas²⁴. The reference film exhibited a surface PSS/PEDOT ratio of 5.28:1, which decreased significantly to 2.38:1 upon Triton X-100 incorporation. This reduction indicates effective suppression of surface-enriched PSS, which is beneficial for improving film morphology, electrical conductivity, and the growth of high-quality perovskite layers²⁵. In addition to enhancing film quality, the reduced PSS content also addresses its intrinsic hygroscopicity, which is known to induce water uptake and interfacial instability during device fabrication²⁶. In this work, the detrimental effect of water uptake is further confirmed, as NBG PSCs based on PEDOT:PSS exhibit degraded performance after

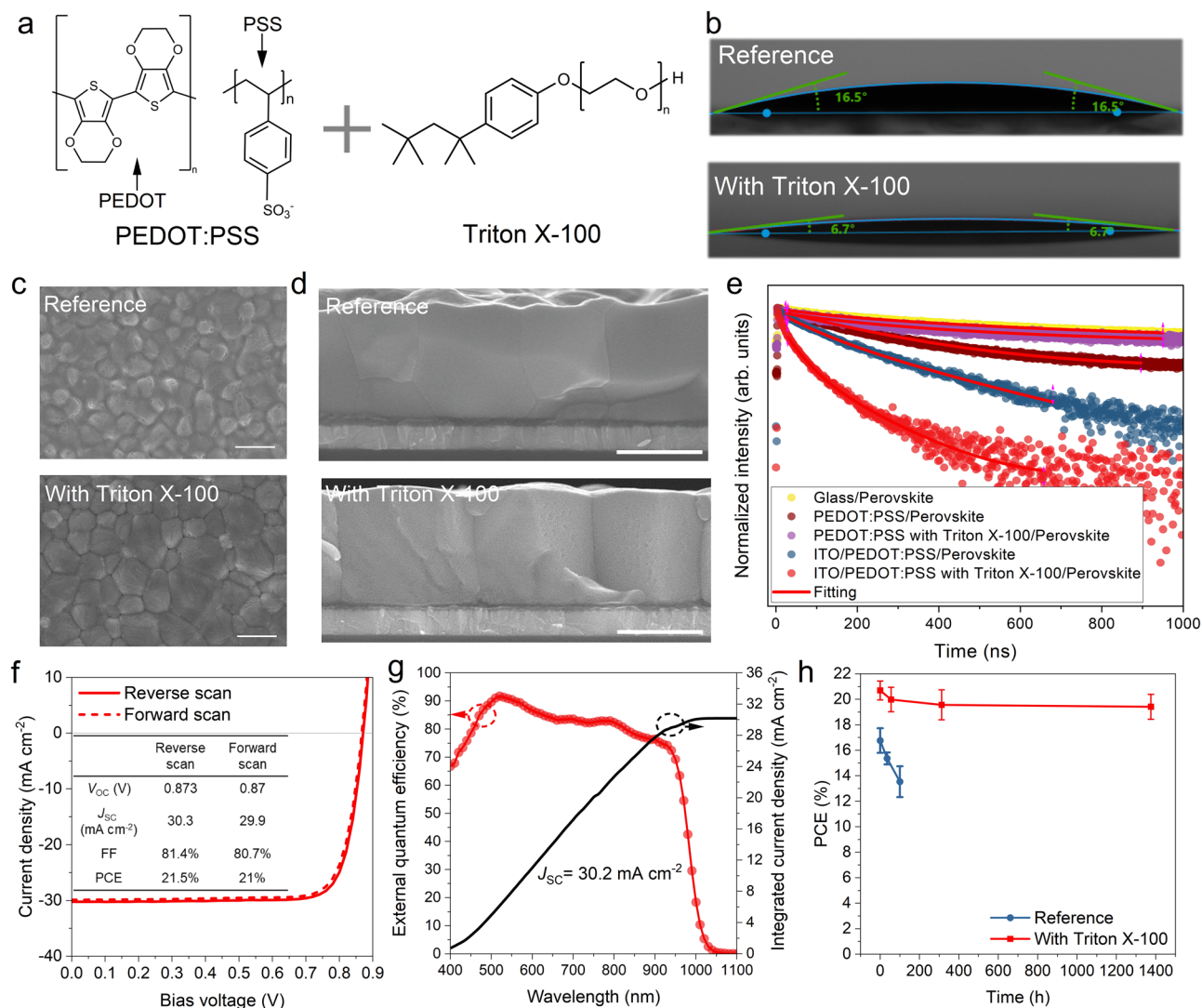


Fig. 2 | The effect of Triton X-100. **a** Chemical structures of PEDOT:PSS and Triton X-100. **b** Contact angle of PEDOT:PSS with or without Triton X-100 on glass/indium tin oxide (ITO). **c** Top-view scanning electron microscopy (SEM) images of perovskite grown on PEDOT:PSS with or without Triton X-100. Scale bars, 1 μm . **d** Cross-sectional SEM images of the perovskite grown on PEDOT:PSS with or without Triton X-100. Scale bars, 500 nm. **e** Time-resolved photoluminescence spectra of perovskite films deposited on bare glass and on PEDOT:PSS layers with or without Triton X-100, as well as on ITO/PEDOT:PSS layers with or without Triton X-100. **f** J - V curves of the champion narrow-bandgap (NBG) perovskite solar cell

(PSCs), the detailed performance parameters are inserted (V_{oc} : open-circuit voltage; J_{sc} : short-circuit current density; FF: fill factor; PCE: power conversion efficiency). **g** External quantum efficiency (EQE) spectrum and integrated J_{sc} of the NBG PSC based on PEDOT:PSS with Triton X-100. By integrating the EQE over the AM 1.5 G standard spectrum, the integrated J_{sc} is 30.2 mA cm^{-2} . **h** The dark shelf stability of the NBG PSCs stored in a N_2 filled glove box. The PCE values are presented as mean \pm standard deviation ($n = 8$ individual cells per group). The error bars denote the standard deviation.

prolonged exposure to ambient air following annealing, as shown in Supplementary Fig. 11.

To further investigate the PSS/PEDOT ratio within the bulk of the film, we performed XPS depth profiling on PEDOT:PSS films. Using an Ar ion gun, the PEDOT:PSS ($\sim 20 \text{ nm}$) film deposited on ITO was sputtered layer by layer, and XPS analysis was performed at each depth. The evolution of the S 2p region with sputtering time is presented in Fig. 3e. Notably, the results reveal that PSS accumulates only near the top surface of the PEDOT:PSS film, while the bulk region is dominated by PEDOT. Our observation indicates a distinct structural arrangement for PEDOT:PSS that differs from the previously assumed “pancake” structure model reported in the literature²⁷. When Triton X-100 is introduced, as shown in Fig. 3f, a substantial reduction in the PSS phase is observed at the top surface of the film. To quantify the overall PSS/PEDOT ratio across the films, we integrated the intensities of the S 2p peaks corresponding to the binding energy ranges for styrene

sulfonate (170–166 eV) and EDOT thiophene (166–161 eV). The atomic ratio of sulfur from PSS decreased from 13.4% in the reference film to 5.4% in the film with Triton X-100. This significant reduction highlights the ability of Triton X-100 to alter the bulk composition of PEDOT:PSS by weakening the ionic interactions between PEDOT and PSS²⁸. Such modulation facilitates the removal or redistribution of excess PSS, ultimately improving the interfacial properties and overall quality of the hole transport layer. XPS depth profiling for the PEDOT:PSS films on PEN/ITO shows a similar trend as shown in Supplementary Fig. 12.

Double-layer structure and dipoles

Through our in-depth investigation of PEDOT:PSS, we uncovered a previously overlooked double-layer structure in ultra-thin PEDOT:PSS films. The addition of Triton X-100 was found to significantly reduce the PSS content in the resulting film, thereby modifying both the interface properties and the subsequent perovskite growth. The

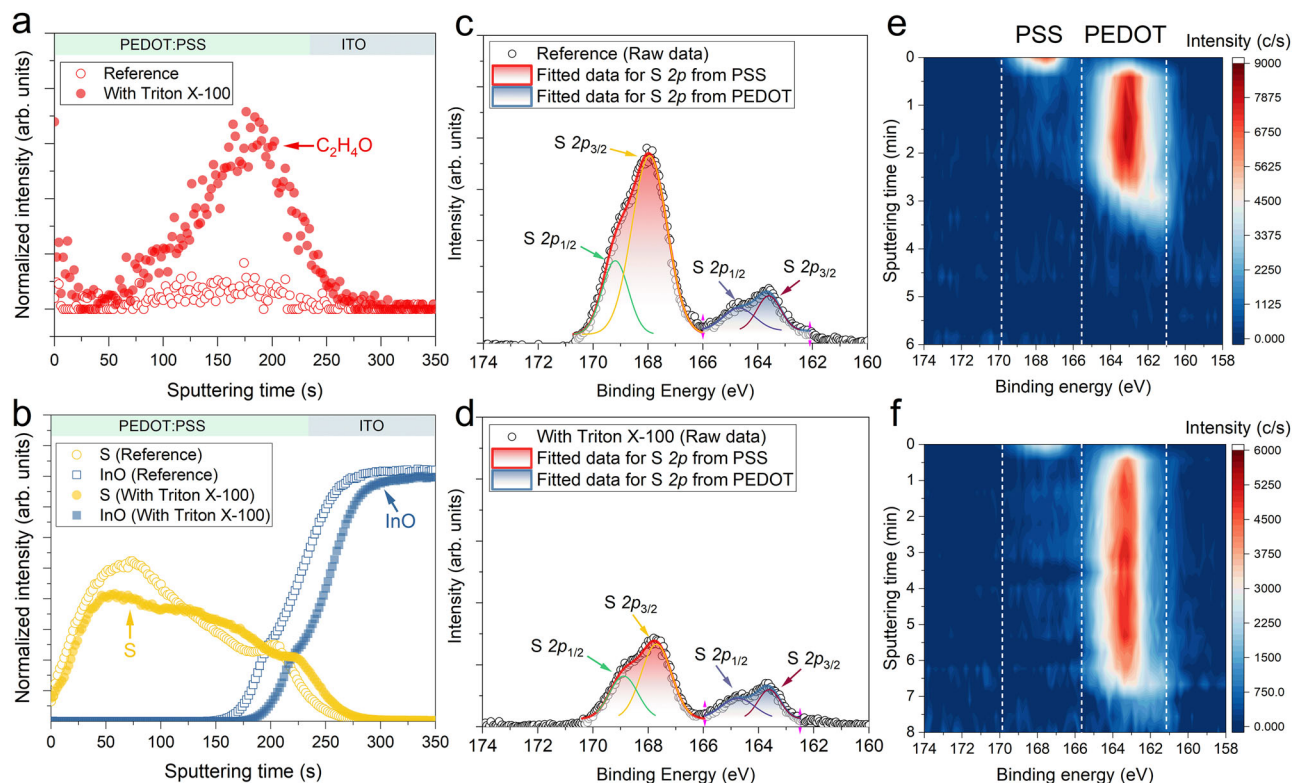


Fig. 3 | Distribution of fragments in PEDOT:PSS. a, b Time-of-flight secondary ion mass spectrometry (ToF-SIMS) depth profiles of C₂H₄O, S, and InO for PEDOT:PSS with or without Triton X-100 on glass/indium tin oxide (ITO). **c, d** X-ray photoelectron spectroscopy (XPS) measurements on the surface of PEDOT:PSS thin film with or without Triton X-100, showing the core level peaks of S 2p. The deconvoluted profiles were fitted with two symmetric/asymmetric Gaussian-Lorentzian

functions representing sulfur atoms from styrene sulfonate (170–166 eV, red gradients) and EDOT thiophene (166–161 eV, navy gradients). **e** S 2p region from XPS depth profiling measurements for pristine PEDOT:PSS thin film and **(f)** for that with Triton X-100. The core level peaks of S 2p for PSS and PEDOT are separated with white dashed line.

formation and impact of this double-layer structure on device performance are explained as follows:

As depicted in Fig. 4a, spin-coating the PEDOT:PSS dispersion led to the formation of a double-layer structure after drying, consisting of a thin PSS layer at the top surface and a thick PEDOT-rich base layer at the bottom. We attribute this phase segregation to the preferential lateral interactions between PEDOT units, which drive PSS segregation toward the surface. When applied to NBG solar cells, the averaged PCE was merely ~13.9%, with poor uniformity across multiple fabrication batches (Fig. 4b). We suspect that the PSS layer poses a current barrier at the buried interface during light soaking and thus leads to decreased performance for the solar cells. By incorporating Triton X-100 into the PEDOT:PSS dispersion prior to the spin-coating process, we observed a significant reduction in the PSS phase amount (as illustrated in Fig. 4c), changing the overall interfacial properties of the PEDOT:PSS layer. As shown in the box chart (Fig. 4d), Triton X-100 enhanced the uniformity of photovoltaic parameters, with an average PCE of ~19.9%, a substantial improvement over the reference group. The improved uniformity was primarily from the improvements in J_{SC} and FF (Supplementary Fig. 13). Electroluminescence mapping of the 1 cm² NBG PSCs further confirmed the improved uniformity of the cells across the substrate (Supplementary Fig. 14). During the formation of the double-layer structure, Triton X-100 likely accelerates the phase segregation by weakening ionic interactions between PEDOT and PSS, thereby reducing the insulating PSS phase in the resultant film²⁸. As detailed in Supplementary Note 2, Triton X-100 associates with PSS, loosening the core-shell structure and increasing the transmittance of the PEDOT:PSS dispersion. It is worth noting that the resulted double-layer structure may represent a unique case in ultra-thin films where the thickness is comparable to or smaller than the core-shell

dimensions, whereas, in thicker films (> 100 nm), previous studies have reported PSS distributed throughout the bulk²⁹.

Although the addition of Triton X-100 to PEDOT:PSS has resulted in improved perovskite growth, it remains unclear whether the enhanced device performance is primarily due to the improved perovskite quality or the modified buried interface properties, specifically the reduced PSS content. To elucidate the role of surface PSS, we conducted post-deposition treatments (PDTs) on reference PEDOT:PSS films using deionized water and Triton X-100, respectively, as illustrated in Fig. 4e. Solar cells processed with these films exhibited treatment-dependent behavior. With the water-washed films, the devices showed a modest improvement in PCE (Fig. 4f), likely resulting from the partial removal of the insulating PSS phase at the surface. Intriguingly, Triton X-100-treated films demonstrated significantly enhanced PCE and improved uniformity (Fig. 4g), primarily due to an increase in J_{SC} (Supplementary Fig. 15). This underscores not only the critical role of this interface but also that Triton X-100 more effectively removes the insulating PSS phase due to its stronger interaction with PSS. To check the effect of Triton X-100 at the ITO/perovskite interface, solar cells were also fabricated using Triton X-100-treated ITO substrates prior to PEDOT:PSS deposition. As the results shown in Supplementary Fig. 16, their performance remained statistically similar to that of the reference group, indicating that the ITO/perovskite interface plays a negligible role. Instead, the buried perovskite/PEDOT:PSS interface emerges as the dominant loss pathway of the devices.

In the traditional “pancake” model, improvements in PEDOT:PSS film quality are typically ascribed to enhanced conductivity resulting from reduced PSS content³⁰. However, with our identification of a vertically segregated double-layer structure in PEDOT:PSS and the observation of abnormal $J-V$ behavior under light soaking, we propose

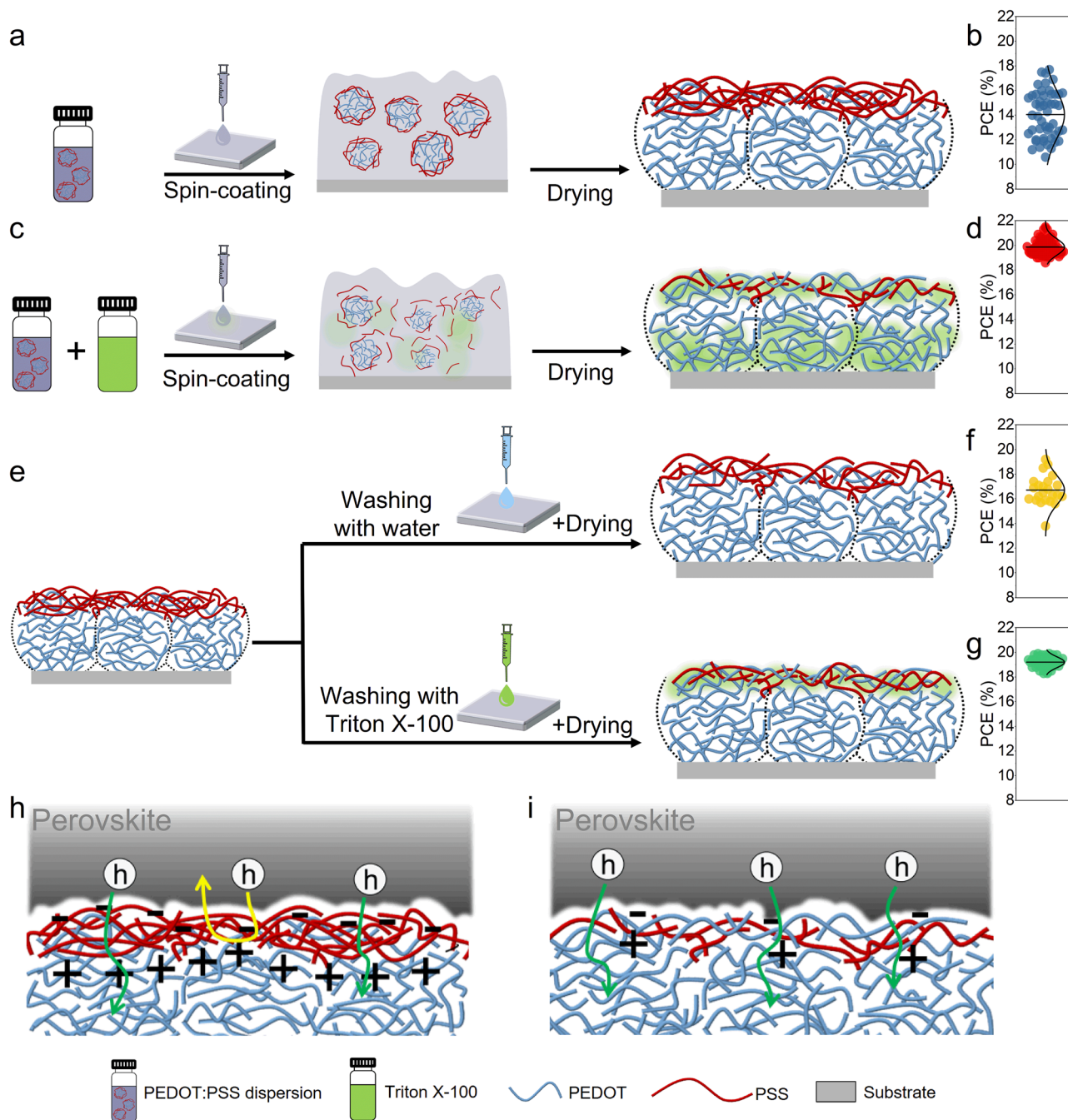


Fig. 4 | Schematics illustrating the formation of double-layer PEDOT:PSS and the resultant device performance. **a** Illustration on the fabrication of reference PEDOT:PSS film and **(b)** corresponding statistical distribution of power conversion efficiency (PCE) for NBG PSCs, 50 cells included. **c** Illustration on the fabrication of PEDOT:PSS film with Triton X-100 and **(d)** corresponding statistical distribution of PCE, 65 cells included. **e** Illustration on the post-deposition treatment (PDT) for the reference PEDOT:PSS films with water or Triton X-100. **f** Statistical distribution of

PCE for NBG PSCs with water wash (**f**, 23 cells included) or **(g)** with Triton X-100 wash on PEDOT:PSS (52 cells included). **h** Illustration on possible electric dipoles forming at the top surface of the reference PEDOT:PSS film, and **(i)** reduced electric dipoles with Triton X-100. In **(b, d, f, g)**, horizontal bars indicate the 25–75 percentile, mean, and minimum/maximum values, respectively. The distribution is fitted with the Gaussian function (solid line).

an additional mechanism involving the intrinsic charge characteristics of the material. PEDOT:PSS is a polyelectrolyte complex composed of positively charged PEDOT chains and negatively charged PSS counterions, bound through electrostatic interactions. We hypothesize that vertical phase segregation gives rise to localized electric dipoles at the interface between the PSS-rich, negatively charged surface layer and the PEDOT-rich, positively charged bottom layer (Fig. 4h). To evaluate this mechanism, we performed drift–diffusion simulations using

SETFOS (Fluxim AG), modeling dipole-induced energy-level shifts at the PEDOT:PSS/perovskite interface; the simulations predict reductions in J_{SC} and fill factor when interfacial dipoles are included, closely matching our experimental trends (Supplementary Note 3). During J – V characterization, this asymmetric charge distribution may become further polarized, enhancing dipole formation at the buried interface. These interfacial dipoles are likely to hinder vertical charge transport—particularly hole extraction from the perovskite into the PEDOT:PSS

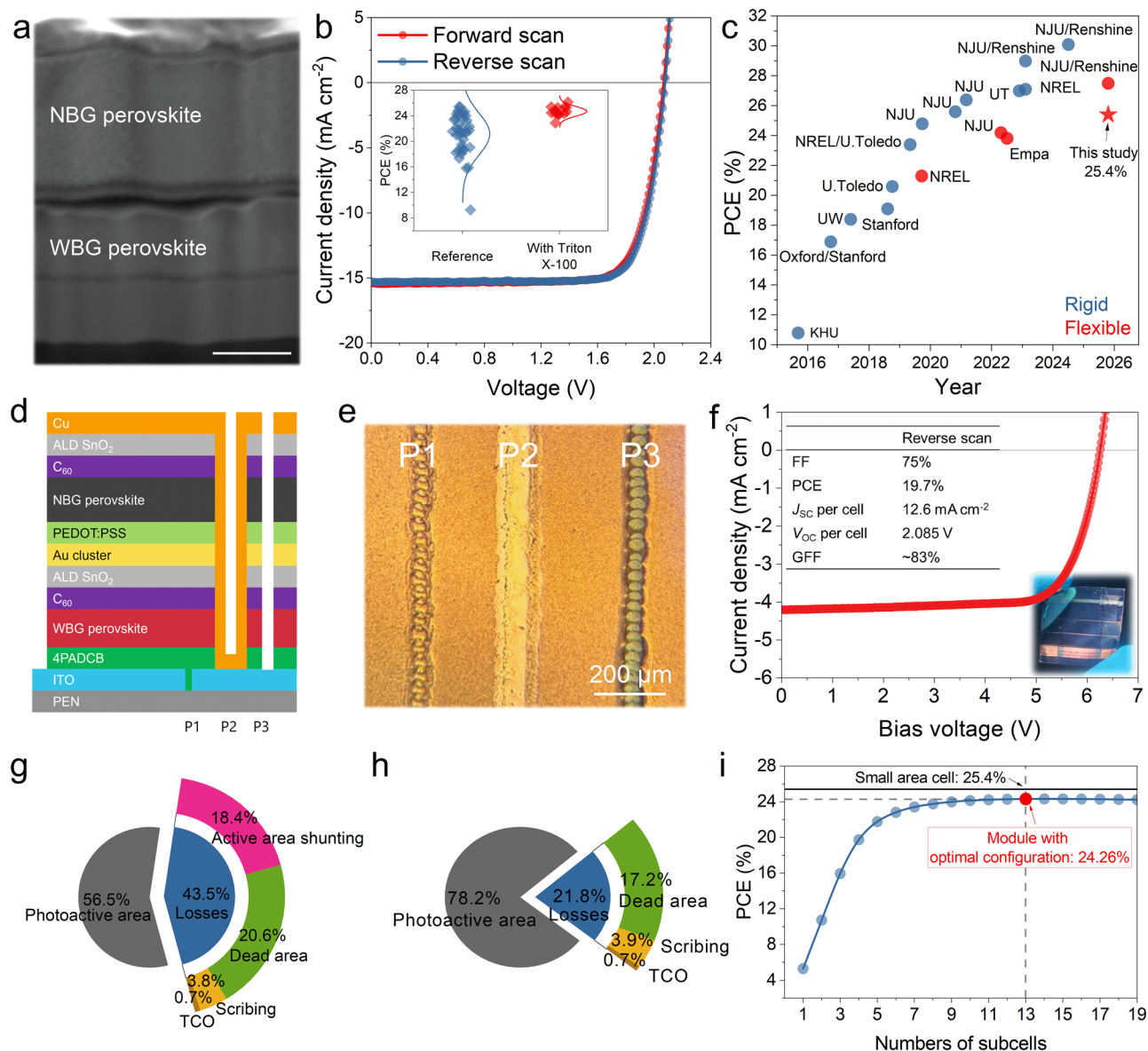


Fig. 5 | Flexible all-perovskite tandem solar cells (TSCs) and mini-modules.

a Focused ion beam scanning electron microscopy (FIB-SEM) image for a flexible TSC. Scale bar: 350 nm. **b** J - V curves for the champion device, and inserted the box chart shows the power conversion efficiencies (PCEs) of 17 and 15 flexible TSCs for the reference group and the group with Triton X-100, respectively. **c** PCE progress for 2T all-perovskite TSCs. Data include this work and a contemporaneous report published during the review of this manuscript³⁴. **d** Schematics illustrate the laser scribes interconnecting the subcells in the tandem solar mini-module. ALD atomic layer deposition, NBG narrow-bandgap, WBG wide-bandgap, ITO indium tin oxide, PEN polyethylene naphthalate. **e** Optical microscope image of scribing lines indicating the P1-P2-P3 interconnections. **f** J - V curve of the champion flexible tandem solar mini-module. The photo of the device is inserted. V_{OC} open-circuit voltage, J_{SC} short-circuit current density, FF fill factor, GFF geometric fill factor. **g** Loss analysis of non-optimized mini-module and **(h)** Optimized mini-module (Laoss, Fluxim). TCO transparent conductive oxide. **i** PCE potential of a 10 cm \times 10 cm flexible tandem solar module based on the layer design and laser scribes with optimized subcell width and dead area, simulated with Laoss (Fluxim).

PEN polyethylene naphthalate. **e** Optical microscope image of scribing lines indicating the P1-P2-P3 interconnections. **f** J - V curve of the champion flexible tandem solar mini-module. The photo of the device is inserted. V_{OC} open-circuit voltage, J_{SC} short-circuit current density, FF fill factor, GFF geometric fill factor. **g** Loss analysis of non-optimized mini-module and **(h)** Optimized mini-module (Laoss, Fluxim). TCO transparent conductive oxide. **i** PCE potential of a 10 cm \times 10 cm flexible tandem solar module based on the layer design and laser scribes with optimized subcell width and dead area, simulated with Laoss (Fluxim).

layer—thereby limiting device performance. Treatment with Triton X-100 mitigates this issue by reducing surface PSS accumulation, weakening dipole formation and thus facilitating more efficient charge extraction (Fig. 4i). This mechanism accounts for the observed enhancement in device performance and uniformity. Collectively, these findings reveal a previously overlooked microstructural and electrostatic aspect of PEDOT:PSS, offering a conceptual framework for optimizing its role in optoelectronic applications.

Flexible tandem solar cells and mini-modules

Leveraging the improved conformal coating of PEDOT:PSS with Triton X-100 and the resulting enhanced performance in single junction

devices, we progressed to the fabrication of high-performance flexible solar cells and mini-modules.

During the processing of flexible TSCs, our finding, illustrated in Supplementary Fig. 17, confirms that the incorporation of Triton X-100 significantly enhances the conformality of the PEDOT:PSS coating on flexible WBG perovskite cells. This improvement provides a robust foundation for the fabrication of flexible tandem devices. With Triton X-100 in PEDOT:PSS, we first fabricated flexible TSCs, and the cross-sectional SEM image is presented in Fig. 5a. We note that the devices processed with Triton X-100 show markedly improved uniformity in PV performance compared to that of the reference devices. Our best-performing device achieves a PCE of 25.4%, with a V_{OC} of 2.08 V, a J_{SC} of

15.27 mA cm⁻², and a FF of 80.2% (Fig. 5b). This is one of the highest efficiencies reported to date for flexible all-perovskite TSCs, as summarized in the efficiency progress shown in Fig. 5c. The EQE spectra for our flexible TSC are shown in Supplementary Fig. 18.

As a further step toward practical applications, we developed a proof-of-concept flexible all-perovskite tandem solar mini-module. Tandems based on blade-coated 5 × 5 cm² flexible WBG cells showed improved performance uniformity with Triton X-100, but the baseline performance is relatively poor, and the uniformity remained insufficient for reliable mini-module fabrication (Supplementary Fig. 19). We therefore used spin-coated 2.5 × 2.5 cm² flexible WBG cells for mini-module development. We adapted the established thin-film module interconnection approach, utilizing three laser-scribed lines to interconnect cells, as depicted in Fig. 5d. While this interconnection schemes were successfully implemented in rigid all-perovskite tandem solar mini-modules in recent years^{9,31–33}, its adaptation to flexible substrates poses significant challenges due to substrate deformation, uneven thermal distribution, and mechanical fragility during laser processing. In this work, laser scribing techniques for flexible tandem solar mini-modules were thoroughly investigated, with the optimized results presented in Fig. 5e. A proof-of-concept flexible all-perovskite tandem solar mini-module achieved a PCE of 19.7%, with a FF of 75%, a V_{OC} of 2.085 V per cell, and an aperture area of ~1.3 cm² (comprising three cell strips with an ~83% geometric fill factor), as shown in Fig. 5f. To assess mechanical and operational stability, we performed bending and lifetime tests (Supplementary Fig. 20). The mini-module retained ~100% of its initial PCE after 2000 manual bending cycles at a 15 mm radius and maintained >83% after 700 cycles during in situ MPP tracking on a motorized bender. Under continuous MPP tracking, performance showed a rapid initial drop over ~30 h, indicating that their operational stability remains limited and requires further optimization.

During the development of laser scribing techniques for flexible all-perovskite tandem solar modules, we employed optoelectronic simulation using (Laoss v4.2 by Fluxim AG (www.fluxim.com/laoss) to analyze loss mechanisms and to guide process optimization. As shown in Supplementary Fig. 21, experimentally obtained $J-V$ curves were accurately reproduced by simulations incorporating multiple loss channels. In non-optimized mini-modules, the dominant losses were attributed to non-ohmic active area shunting (~18.4%) and dead area losses (~20.6%). The former originated primarily from non-uniform deposition of functional layers, while the latter was mainly due to suboptimal laser scribing quality and layout design (Fig. 5g). Further simulations revealed that poor P2 scribing significantly impacts the FF, while shunting behavior—linked to layer inhomogeneities and interfacial defects—limits the V_{OC} (Supplementary Figs. 22 and 23). After improving film uniformity and optimizing P2 scribing parameters, the active-area shunting loss was significantly mitigated. In the optimized mini-module, the primary remaining loss was associated with the dead area (~17.2%) (Fig. 5h).

Based on our layer design and laser scribing techniques, we simulated the performance of a flexible tandem solar module on a 10 cm × 10 cm substrate with minimized active shunting losses, reduced laser scribing losses, and optimized stripe widths, as shown in Fig. 5i. Our simulation predicts that, with improved uniformity across a large area, a PCE exceeding 24% can be achieved using the laser scribing and layer stacks developed in this study, with a small cell-to-module loss less than 1.5%, showing the great potential of this technology. Concurrently, a related study reported a 23% PCE on a 20.26 cm² flexible all-perovskite tandem mini-module, underscoring the rapid pace of progress in this area³⁴.

Discussion

In summary, we systematically investigated the intrinsic properties and limitations of PEDOT:PSS in high-performance NBG PSCs and

flexible all-perovskite TSCs. We reveal that ultra-thin PEDOT:PSS films spontaneously adopt a vertically segregated double-layer structure, comprising an insulating, PSS-rich surface atop a conductive PEDOT-rich base. This vertical phase separation generates localized electric dipoles at the PEDOT:PSS–perovskite interface, significantly impeding hole extraction. By incorporating the non-ionic surfactant Triton X-100 into the PEDOT:PSS dispersion, we suppress surface PSS accumulation and thereby mitigate dipole-induced extraction barriers—resulting in substantial improvements in device efficiency and reproducibility. Using this strategy, we achieved a high PCE of 25.4% in flexible TSCs. Furthermore, by addressing laser scribing challenges specific to flexible substrates through simulation-guided process refinement, we demonstrate a proof-of-concept flexible all-perovskite tandem solar mini-module with a PCE of 19.7%, projecting achievable module efficiencies exceeding 24% for optimized 10 cm × 10 cm device layouts. Our findings provide fundamental insights into interfacial phenomena within PEDOT:PSS, establishing critical guidelines for advancing flexible all-perovskite tandem photovoltaic technologies.

Methods

Materials

Pre-patterned indium tin oxide (ITO) coated glass (15 Ω/sq) or polyethylene naphthalate (PEN) (12 Ω/sq) were purchased from Advanced Election Technology Co., Ltd. Lead (II) iodide (PbI₂, 99.99%), cesium iodide (CsI, 99%), methylammonium iodide (MAI, 98%), methylammonium bromide (MABr, ≥98%), were purchased from Tokyo Chemical Industry Co., Ltd. 4PADCB was purchased from Luminescence Technology Corp. Formamidinium iodide (FAI, >99.99%), 2-thiopheneethylammonium chloride (TEACl) was purchased from Greatcell Solar Materials Pty Ltd. Dimethylformamide (DMF, anhydrous, 99.8%), dimethyl sulfoxide (DMSO, anhydrous, ≥99.9%), chlorobenzene (CB, anhydrous, 99.8%), chloroform (CF, anhydrous, 99.8%), isopropanol (IPA, anhydrous, ≥99.9%), toluene (anhydrous, 99.8%), lead (II) bromide (PbBr₂, 99.999%), tin (II) iodide (SnI₂, 99.99%), ammonium thiocyanate (NH₄SCN, 99.99%), tin (II) fluoride (SnF₂, 99%), copper (Cu, 99.99%), Glycin-hydrochlorid (GlyHCl, ≥99.9%), Triton™ X-100 (~10% in H₂O), Ethylenediammonium diiodide (EADI₂, ≥98.0%) were purchased from Sigma-Aldrich Pty Ltd. Ethanol (anhydrous, ≥99.9%) was purchased from VWR International, LLC. [6,6]-Phenyl-C61-butyric acid methyl ester (PCBM), fullerene-C₆₀ and bathocuproine (BCP) were purchased from Xi'an Yuri Solar Co., Ltd. PEDOT:PSS (Clevios PVP AI 4083) was purchased from Heraeus Epurio LLC. All the materials were used as received.

Solar cells fabrication

Device fabrication for NBG PSCs: The pre-patterned ITO substrates were soaked in detergent (1% water solution of Hellmanex® III) and then cleaned by sonication for 10 min with deionized water and isopropanol sequentially. After drying with N₂ flow, the substrates were further cleaned by UV/Ozone treatment (Jelight Company Inc.) for 30 min. PEDOT:PSS dispersion (Triton X-100) were added to the dispersion according to different weight ratios) was filtered with a 0.45 μm polyvinylidene difluoride (PVDF) filter, then coated on the cleaned ITO substrate at 4000 rpm for 50 s and annealed at 140 °C for 20 min. The substrates were then transferred to an N₂-filled glove box for perovskite film fabrication. 1.8 M Cs_{0.1}FA_{0.6}MA_{0.3}Sn_{0.5}Pb_{0.5}I₃ perovskite precursor were prepared by dissolving NH₄SCN (5.46 mg), GlyHCl (8.03 mg), SnF₂ (28.21 mg), CsI (93.53 mg), FAI (371.46 mg), MAI (171.69 mg), SnI₂ (670.53 mg), and PbI₂ (829.81 mg) into a mixed solvent of DMF (1500 μL) and DMSO (500 μL). The molar ratio of NH₄SCN:GlyHCl:SnF₂:CsI:FAI:MAI:SnI₂:PbI₂ is 0.036:0.036:0.09:0.18:1.08:0.54:0.9:0.9. Before spin-coating, the precursor was filtered with a 0.22 μm polytetrafluoroethylene (PTFE) filter. The precursor was spin-coated onto ITO/PEDOT:PSS by a two-step spin-coating. The first step is 1000 rpm for 10 s with a ramp-up of 200 rpm s⁻¹. The second step is

4000 rpm for 40 s with a ramp-up of 2000 rpm s⁻¹. CB (400 μL) was dropped onto the spinning substrate at the 20 s of the second step. The substrate was then annealed at 100 °C for 10 min and 65 °C for 5 min. For a PDT with EDAl₂³⁵, 1.0 mg EDAl₂ was added to 1.0 mL IPA and 1.0 mL toluene. The mixed solvent solution was stirred overnight and then filtered through a 0.22 μm PTFE filter. EDAl₂ solution was spin-coated onto the perovskite film at 4000 rpm for 20 s with a ramp-up of 1333 rpm s⁻¹, followed by an annealing at 100 °C for 2 min. All the substrates were then transferred into a vacuum chamber for thermal evaporation. C₆₀ (23 nm)/BCP (7 nm)/Cu (100 nm) were sequentially deposited on the substrates to complete the solar cell. For each substrate, there are four cells. The designed contact area of each device is 0.1024 cm². The illuminated area of the device was defined with a patterned mask (0.09 cm²). Devices were encapsulated with cover glass and UV-curable epoxy. All the procedures were carried out in a N₂-filled glove box except the spin-coating and annealing of PEDOT:PSS.

Device fabrication for WBG PSCs: Pre-patterned PEN/ITO substrates were first fixed onto rigid glass substrates with UV epoxy and then cleaned with ethanol and dried with N₂ flow. Before device fabrication, the substrates were further cleaned by UV/Ozone treatment for 30 min. 4PADCB precursor (0.3 mg mL⁻¹ in ethanol, preheated at 40 °C) was spin-coated onto the cleaned ITO substrates at 3000 rpm for 30 s after 30 s resting on the substrate, followed by an annealing at 100 °C for 2 min. 1.2 M Cs_{0.12}FA_{0.8}MA_{0.08}PbI_{1.8}Br_{1.2} precursor was prepared by dissolving MABr (21.50 mg), CsI (74.83 mg), FAbR (95.98 mg), FAI (198.11 mg), PbBr₂ (352.33 mg) and PbI₂ (663.85 mg) into a mixed solvent of DMF (1600 μL) and DMSO (400 μL). The molar ratio of MABr:CsI:FAbR:FAI:PbBr₂:PbI₂ is 0.08:0.12:0.32:0.48:0.4:0.6. Before spin-coating, the precursor was filtered with a 0.22 μm PTFE filter. The precursor was spin-coated onto ITO/SAM by a two-step spin-coating. The first step is 2000 rpm for 10 s with a ramp-up of 200 rpm s⁻¹. The second step is 6000 rpm for 40 s with a ramp-up of 2000 rpm s⁻¹. CB (300 μL) was dropped onto the spinning substrate at the 20 s of the second step. The substrates were then annealed at 60 °C for 2 min and 100 °C for 7 min. For TEACl PDT⁷, TEACl in IPA (0.5 mg mL⁻¹) is spin-coated onto the perovskite film at 3000 rpm for 30 s, followed by an annealing at 100 °C for 3 min. After cooling, PCBM in CF (20 mg mL⁻¹) right after filtering with a 0.22 μm PTFE filter was spin-coated at 3000 rpm for 50 s, followed by annealing at 100 °C for 5 min. The substrates were then transferred to an atomic layer deposition (ALD) chamber for SnO_x deposition (~20 nm) at relatively low temperature (100 °C) by periodic pulse of tetrakis(dimethylamino) tin(IV) (99.9999%, Nanjing Ai Mou Yuan Scientific Equipment Co., Ltd) and deionized water. Thereafter, the substrates were then transferred into vacuum chamber for the thermal evaporation of Cu (100 nm). For each substrate, there are four cells. The designed contact area of each device is 0.1024 cm². The illuminated area of the cell was defined with a patterned mask (0.09 cm²). All spin coatings were carried out in an N₂-filled glove box.

Device fabrication for monolithic TSCs and TSMs: For TSCs, all the procedures are the same for the flexible WBG cell until ALD-SnO_x is finished. The substrates were then transferred to the magnetron sputtering system to sputter 100 nm IZO at a 30 W power under an Ar pressure of 0.4 Pa. Then, PEDOT:PSS diluted with IPA (volume ratio 1:1) was spin-coated onto the sputtered IZO substrates at 4000 rpm for 50 s and then annealed at 100 °C for 5 min in air. The other steps to fabricate monolithic TSCs were consistent with those of the fabrication of NBG PSCs. For TSMs, the substrates were first processed with P1 laser scribing before cleaning. When the ALD-SnO_x for WBG cell was finished, the substrates were transferred into a vacuum chamber for thermal evaporation of Au (1.5 nm). In addition, the BCP layer in the NBG cell was replaced by ALD-SnO_x for better protection, followed by a P2 laser scribing. And P3 laser scribing was performed after Cu deposition. The other steps to fabricate monolithic tandem solar

modules were consistent with those of the fabrication of NBG PSCs. All the laser scribing processes were done in the ambient air.

Laser scribing for the modules: Laser scribing was performed on a TruMark Station 5000, using a nanosecond pulsed Nd:YVO₄ laser with a wavelength of 355 nm.

Characterizations

Contact angle measurements, SEM and TrPL: Contact angle measurements were carried out on a drop shape analyzer (Krüss, DSA30E). The SEM images were taken with a Hitachi S-4800 Scanning Electron Microscope using 5–10 kV acceleration voltage. TrPL was measured using the MicroTime 100 system from PicoQuant. A 639 nm pulsed laser diode (pulse width at ~100 ps) was used. The laser pulse frequency was 0.5 MHz. For the fitting procedure, a biexponential decay was used.

ToF-SIMS: Element depth profiles were obtained with a time-of-flight secondary ion mass spectrometer (ToF-SIMS V system, ION-TOF). The primary beam was 25 keV Bi³⁺ with a total current of 0.41 pA and a raster size of 50 × 50 μm². Cs⁺ ions were used with 1000 eV ion energy, 15 nA pulse current on a 400 × 400 μm² raster size to bombard and etch the film. The data were plotted with the intensity for each signal normalized to the total counts of the signal.

XPS: XPS were performed using the ULVAC-PHI PHI 5000 Versaprobe III system. The analyses were conducted under ultra-high vacuum conditions at a pressure of 10⁻⁷ to 10⁻⁸ Pa. A LaB6 filament served as the source for the electron beam, which was subsequently focused by an electrostatic lens and directed onto an aluminum anode by modulating the voltages on the scanning plates. The interaction between the electron beam and the aluminum anode at a power of 50 W and a voltage of 15 kV generated a monochromatic X-ray beam. This beam, with a spot size of 20 μm, was reflected and used as the source beam for sample analysis.

The system's 180° spherical capacitor energy analyzer, equipped with a multichannel detector, provided an energy resolution of ≤0.5 eV at the Ag 3 d_{5/2} peak. Electron and ion charge neutralizers were employed to mitigate surface charging effects during XPS measurements. Depth profiling was achieved by etching the sample surface with a 2 kV Ar⁺ ion beam over a 2 mm × 2 mm area between measurements. Spectrum curve fitting was carried out using MultiPak software, applying Shirley-background subtraction and fitting the data with a Gaussian-Lorentzian function.

FIB-SEM: SEM (Thermo Fisher Scientific, Scios 2 DualBeam) studied the microstructure of the flexible all-perovskite TSC stack. In a high vacuum (~10⁻⁶ mbar), a cross-section was roughly milled with an ion beam current of 1 nA, followed by a cleaning cut with an ion beam current of 100 pA at 30 kV.

Electroluminescence: Device spatial homogeneity was characterized by electron luminescence measurements using a CCD camera (300–1000 nm spectra response, ORCA-ER C4742-80-12AG, HAMAMASU) and a Keithley 2450 source meter by applying a constant voltage of 0.9 V through the devices.

J-V and EQE characteristics: Current density-voltage (*J-V*) characteristics were measured in four-contact mode at standard test conditions (100 mW cm⁻²) using a Keithley 2400 source meter. A solar simulator (ABA class, LOT-QuantumDesign) was calibrated to AM 1.5 G one sun illumination using a certified monocrystalline silicon solar cell (RS-ID-5, Fraunhofer-ISE). The solar cells were measured with an aperture mask with an aperture area of 0.09 cm² (1.3 cm² for the modules). The *J-V* measurements were performed in forward and reverse directions. The cells were measured with a scan rate of 100 mV/s (using an integration time of 0.1 s and a delay of 0.1 s for each data point, the voltage step was 0.02 V). The steady-state efficiency as a function of time was recorded using an MPP tracker, which adjusts the applied voltage to reach the maximum power point (perturb and observe algorithm). The external quantum efficiency of the solar cells

was measured with a lock-in amplifier. The probing beam was generated by a chopped white source (900 W, halogen lamp, 280 Hz) and a dual grating monochromator. The beam size was adjusted to ensure an illumination area within the cell area. A certified single-crystalline silicon solar cell was used as a reference cell. White bias light was applied during the measurement with an intensity of ~0.1 sun. The EQE characterizations of the TSCs were conducted using an EQE setup (QE-R, Enlitech). The bias illumination from a 150 W white lamp was filtered with 550 and 850 nm optical filters for the measurement of bottom and top subcells' responses, respectively. Both *J-V* and EQE characteristics are measured under ~25 °C in ambient air. The shelf stability of encapsulated NBG PSCs was evaluated via repeated *J-V* measurements over time, and the devices were stored in an N₂-filled glovebox between measurements.

Bending test: The mechanical bending test is done by manually conforming the mini-modules to the mold with a radius of 15 mm. For the MPP tracking during the bending, the sample is fixed onto the stages of a customized bending machine, and as the distance between the two stages becomes shorter, bending stress is applied to the device fixed to the stages during the MPP tracking. To preserve flexibility and protect the devices, the flexible tandem mini-modules were encapsulated using a desktop laminator (Fellowes Laminiergerät Caliber) with double sided PET foil (80 micrometers for each) at a temperature of 125 °C. (Supplementary Note 4 details the bending test and its visualization).

Operational stability: Light-soaking stability test was done by continuous MPP tracking of the encapsulated tandem solar mini-modules under simulated 1 sun illumination (using white light-emitting diode (LED) solar simulator with intensity equivalent to 100 mW cm⁻²) in a 300 mbar N₂ chamber (purged for three times with N₂). No active cooling is applied, and the device temperature rose to ~42 °C during operation due to the heating effect of light illumination. Because the current encapsulation is not yet sufficiently robust for moisture- and oxygen-sensitive devices under prolonged light/thermal stress, these MPP data should be regarded as preliminary; improved encapsulation will be implemented to enable systematic, long-term operational-stability testing.

Reporting summary

Further information on research design is available in the Nature Portfolio Reporting Summary linked to this article.

Data availability

All data supporting the findings of this study are available within the article and its supplementary files. Any additional requests for information can be directed to and will be fulfilled by the corresponding authors. Source data are provided in this paper.

References

- Albrecht, S. & Rech, B. Perovskite solar cells: On top of commercial photovoltaics. *Nat. Energy* **2**, 16196 (2017).
- Wang, R. et al. Prospects for metal halide perovskite-based tandem solar cells. *Nat. Photonics* **15**, 411–425 (2021).
- Green, Martin A. et al. Solar cell efficiency tables (Version 65). *Prog. Photovolt.: Res. Appl.* **33**, 3–15 (2025).
- Zhang, J., Zhang, W., Cheng, H.-M. & Silva, S. R. P. Critical review of recent progress of flexible perovskite solar cells. *Mater. Today* **39**, 66–88 (2020).
- Holzhey, P., Prettl, M., Collavini, S., Chang, N. L. & Saliba, M. Toward commercialization with lightweight, flexible perovskite solar cells for residential photovoltaics. *Joule* **7**, 257–271 (2023).
- Li, L. et al. Flexible all-perovskite tandem solar cells approaching 25% efficiency with molecule-bridged hole-selective contact. *Nat. Energy* **7**, 708–717 (2022).
- Lai, H. et al. High-performance flexible all-perovskite tandem solar cells with reduced VOC-deficit in wide-bandgap subcell. *Adv. Energy Mater.* **12**, 2202438 (2022).
- Shang, Y. et al. Synchronous defect passivation of all-inorganic perovskite solar cells enabled by fullerene interlayer. *Nano Res. Energy* **2**, e9120073 (2023).
- Abdollahi Nejand, B. et al. Scalable two-terminal all-perovskite tandem solar modules with a 19.1% efficiency. *Nat. Energy* **7**, 620–630 (2022).
- Modarresi, M. & Zozoulenko, I. Why does solvent treatment increase the conductivity of PEDOT: PSS? Insight from molecular dynamics simulations. *Phys. Chem. Chem. Phys.* **24**, 22073–22082 (2022).
- Nardes, A. M. et al. Microscopic understanding of the anisotropic conductivity of PEDOT:PSS Thin Films. *Adv. Mater.* **19**, 1196–1200 (2007).
- Lang, U., Müller, E., Naujoks, N. & Dual, J. Microscopical investigations of PEDOT:PSS thin films. *Adv. Funct. Mater.* **19**, 1215–1220 (2009).
- Yan, F., Parrott, E. P. J., Ung, B. S. Y. & Pickwell-MacPherson, E. Solvent doping of PEDOT/PSS: effect on terahertz optoelectronic properties and utilization in terahertz devices. *J. Phys. Chem. C* **119**, 6813–6818 (2015).
- Kee, S. et al. Controlling molecular ordering in aqueous conducting polymers using ionic liquids. *Adv. Mater.* **28**, 8625–8631 (2016).
- de Izarra, A., Park, S., Lee, J., Lansac, Y. & Jang, Y. H. Ionic liquid designed for PEDOT:PSS conductivity enhancement. *J. Am. Chem. Soc.* **140**, 5375–5384 (2018).
- Vosgueritchian, M., Lipomi, D. J. & Bao, Z. Highly conductive and transparent PEDOT:PSS films with a fluorosurfactant for stretchable and flexible transparent electrodes. *Adv. Funct. Mater.* **22**, 421–428 (2012).
- Wu, X., Liu, J. & He, G. A highly conductive PEDOT:PSS film with the dipping treatment by hydroiodic acid as anode for organic light emitting diode. *Org. Electron.* **22**, 160–165 (2015).
- Scheer, R. & Schock, H.-W. 305–314 (Wiley-VCH, Weinheim, 2011).
- He, R. et al. Improving interface quality for 1-cm² all-perovskite tandem solar cells. *Nature* **618**, 80–86 (2023).
- Li, J.-W., Huang, B.-S., Chang, C.-H. & Chiu, C.-W. Advanced electrospun AgNPs/rGO/PEDOT:PSS/TPU nanofiber electrodes: Stretchable, self-healing, and perspiration-resistant wearable devices for enhanced ECG and EMG monitoring. *Adv. Compos. Hybrid. Mater.* **6**, 231 (2023).
- Ummadisingu, A. et al. The effect of illumination on the formation of metal halide perovskite films. *Nature* **545**, 208–212 (2017).
- Bi, D. et al. Polymer-templated nucleation and crystal growth of perovskite films for solar cells with efficiency greater than 21%. *Nat. Energy* **1**, 16142 (2016).
- Zhao, Y. et al. Perovskite seeding growth of formamidinium-lead-iodide-based perovskites for efficient and stable solar cells. *Nat. Commun.* **9**, 1607 (2018).
- Crispin, X. et al. The origin of the high conductivity of poly(3,4-ethylenedioxythiophene)-poly(styrenesulfonate) (PEDOT-PSS) plastic electrodes. *Chem. Mater.* **18**, 4354–4360 (2006).
- Zhu, J. et al. Custom-tailored hole transport layer using oxalic acid for high-quality tin-lead perovskites and efficient all-perovskite tandems. *Sci. Adv.* **10**, ead12063 (2024).
- Kim, S.-M. et al. Influence of PEDOT:PSS crystallinity and composition on electrochemical transistor performance and long-term stability. *Nat. Commun.* **9**, 3858 (2018).
- Rivnay, J. et al. Structural control of mixed ionic and electronic transport in conducting polymers. *Nat. Commun.* **7**, 11287 (2016).
- Yoon, S.-S. & Khang, D.-Y. Roles of Nonionic Surfactant Additives in PEDOT:PSS Thin Films. *J. Phys. Chem. C* **120**, 29525–29532 (2016).

29. Lim, K. et al. Improving Electrical Conductivity of PEDOT:PSS with Phase Separation by Applying Electric Fields. *Bull. Korean Chem. Soc.* **39**, 469–476 (2018).
30. Kim, N. et al. Highly conductive PEDOT:PSS nanofibrils Induced by Solution-Processed Crystallization. *Adv. Mater.* **26**, 2268–2272 (2014).
31. Xiao, K. et al. Scalable processing for realizing 21.7%-efficient all-perovskite tandem solar modules. *Science* **376**, 762–767 (2022).
32. Sun, H. et al. Scalable solution-processed hybrid electron transport layers for efficient all-perovskite Tandem Solar Modules. *Adv. Mater.* **36**, 2308706 (2024).
33. Gao, H. et al. Homogeneous crystallization and buried interface passivation for perovskite tandem solar modules. *Science* **383**, 855–859 (2024).
34. Li, M. et al. In situ coating strategy for flexible all-perovskite tandem modules. *Nat. Photonics* **19**, 1255–1263 (2025).
35. Hu, S. et al. Optimized carrier extraction at interfaces for 23.6% efficient tin–lead perovskite solar cells. *Energy Environ. Sci.* **15**, 2096–2107 (2022).

Acknowledgements

This work has received funding from the European Union’s Horizon Europe research and innovation program under grant agreement No 101075605 (F.F.). This work has also been financially supported by the Swiss National Science Foundation (grant no. 200021_213073, F.F.) and Swiss Federal Office of Energy (SFOE, grant no. SI/502549-01, F.F.). The authors acknowledge the financial support from National Science and Technology Council, Taiwan R.O.C. (No. 113-2636-E-007-006, T.L.). We also acknowledge the financial support of projects IMPULZ (IM-2023-82), APVV-21-0297, and APVV-24-0321 (N.M., P.S.). H.L. thanks the funding of the China Scholarship Council (CSC) from the Ministry of Education of P.R. China. The authors gratefully acknowledge Dr. Radha Krishnan Kothandaraman for his kind support in the experimental work, especially for his expertise and assistance in the ALD process.

Author contributions

F.F. and H.L. conceived the idea. H.L. performed most of the sample preparation (NBG, WBG PSCs, TSCs, TSMs, and films), characterizations, and analysis. J.Z. and C.C. helped in fabricating flexible all-perovskite TSCs. R.K. and T.L. performed XPS measurements and analysis. U.A. conducted simulation work and analysis on flexible tandem solar mini-modules. Z.L. and C.S. helped with FIB-SEM characterization. N.M. and P.S. performed GIWAXS measurements and analysis. J.L. performed contact angle measurements and helped in blade-coating flexible WBG

PSCs. P.W. conducted preliminary verification experiments. S.S. helped to develop laser-scribing techniques. H.L. wrote the original manuscript, and all authors contributed to reviewing and editing the manuscript. F.F. directed the overall research. A.N.T., D.Z., and F.F. supervised the project.

Competing interests

The authors declare no competing interests.

Additional information

Supplementary information The online version contains supplementary material available at <https://doi.org/10.1038/s41467-025-66479-0>.

Correspondence and requests for materials should be addressed to Tzu-Ying Lin, Dewei Zhao or Fan Fu.

Peer review information *Nature Communications* thanks Hairen Tan, and the other anonymous reviewer(s) for their contribution to the peer review of this work. A peer review file is available.

Reprints and permissions information is available at <http://www.nature.com/reprints>

Publisher’s note Springer Nature remains neutral with regard to jurisdictional claims in published maps and institutional affiliations.

Open Access This article is licensed under a Creative Commons Attribution-NonCommercial-NoDerivatives 4.0 International License, which permits any non-commercial use, sharing, distribution and reproduction in any medium or format, as long as you give appropriate credit to the original author(s) and the source, provide a link to the Creative Commons licence, and indicate if you modified the licensed material. You do not have permission under this licence to share adapted material derived from this article or parts of it. The images or other third party material in this article are included in the article’s Creative Commons licence, unless indicated otherwise in a credit line to the material. If material is not included in the article’s Creative Commons licence and your intended use is not permitted by statutory regulation or exceeds the permitted use, you will need to obtain permission directly from the copyright holder. To view a copy of this licence, visit <http://creativecommons.org/licenses/by-nc-nd/4.0/>.

© The Author(s) 2025